



OPEN Failure mechanism of a loess slope under extreme rainfall through a model test study of Shixiakou, Lanzhou

Yanan Li¹, Yingmin Xin¹, Mingming Tong¹, Qiguang Zhu¹, Yanjun Hou^{2,3}, Guoxuan Ding⁴, Jinwen Liu^{2,3} & Ping Liu¹✉

Loess landslides are one of the most important natural hazards among various landslide types in China, and rainfall is the main factor triggering loess slope instability. To gain deeper insights into the processes behind slope failure triggered by precipitation, this study conducted an indoor slope rainfall modelling test based on the case of the Shixiakou landslide in Jinzhou, Lanzhou. The test employed a custom-built rainfall simulation device, precisely controlling rainfall intensity and duration to mimic natural rainfall conditions. Soil moisture sensors, pore-water pressure transducers, and strain gauges were strategically installed within the loess slope model to monitor soil moisture dynamics, pore-water pressure variations, and lateral stress distribution in real-time. This investigation examined the progressive failure mechanism of loess slopes under rainfall infiltration through integrated monitoring. The experimental results demonstrate that sustained precipitation triggers a sequential failure process characterized by four distinct phases: initial surface scouring, subsequent basal slope instability, progressive mid-slope shear failure, and ultimate crown section collapse, and finally traction failure mode. It is worth noting that cracks play a crucial role in slope failure by creating preferential channels for water infiltration and subsequent failure development.

Keywords Loess slope, Rainfall induced, Failure mode, Instability mechanism, Fissure evolution

China is recognized as one of the countries most severely affected by landslide geological disasters worldwide. Annual landslide occurrences account for approximately 70% of the nation's total geological disasters¹. With rainfall-induced slope failures constituting a significant proportion. Statistical data indicate that about 70% of landslides are rainfall-triggered, and up to 95% occur during the rainy seasons^{2,3}. These disasters pose substantial threats to infrastructure development and residential safety, consequently garnering considerable attention in the engineering community and stimulating extensive research effort^{4–6}. Among various landslide types, loess landslides exhibit particularly complex deformation and failure mechanisms, especially under rainfall conditions. Therefore, investigating the deformation and failure evolution characteristics of loess landslides under rainfall is crucial for developing effective treatment and early warning systems, ultimately reducing disaster occurrences.

Numerous scholars have conducted extensive research on rainfall-induced landslide mechanisms and evolution characteristics through indoor slope model tests and theoretical analyses. Regarding investigations into failure modes and macroscopic mechanisms, studies have primarily elucidated various failure patterns and evolutionary behaviors under differing conditions. Li et al.⁷ examined erosion mechanisms and control strategies for steep loess slopes employing combined experimental and optimization methodologies, while Xue et al.⁸ utilized model equations to analyze infiltration rates in partially saturated soil slopes. Chang et al.⁹ investigated the failure modes of loess fill slopes under rainfall conditions via physical modeling. Wu et al.¹⁰ elucidated a multi-stage retrogressive failure mechanism initiating from the slope toe through experimental and simulation approaches. Yao et al.¹¹ and Tang et al.¹² systematically examined slope responses under varied parametric conditions through comprehensive model testing. Wang and Sassa^{13,14} conducted multiple flume

¹Key Laboratory of Mechanics on Disaster and Environment in Western China, College of Civil Engineering and Mechanics, Lanzhou University, Lanzhou 730000, China. ²Institute of Geo-environmental Monitoring of Gansu Province, Lanzhou 730050, China. ³Observation and Research Station of Urban Geological Hazard in Lanzhou, Ministry of Natural Resources, Lanzhou 730050, China. ⁴Technology Innovation Center for Geohazard Monitoring and Early Warning in Gansu Province, Institute of Engineering Geology, Lanzhou 730000, China. ✉email: liuping@lzu.edu.cn

experiments to analyze the effects of soil particle size and fine content on slope failure during rainfall infiltration. Wang et al.¹⁵ identified “sliding-flow” and “flow-sliding” failure mechanisms in rainfall-induced loess landslides, whereas Wu et al.⁵ and Li et al.¹⁶ performed specialized model tests focusing on infiltration effects and stratified soil slopes, respectively. Concerning the influence of preferential flow and fissures, research has emphasized the dominant role of non-uniform water infiltration. Ren et al.¹⁷ demonstrated through model tests that tension cracks form U-shaped preferential infiltration zones, while Ma et al.¹⁸ established through field investigations that preferential flow infiltration rates exceed uniform flow by factors of 2 to 12, substantially altering internal moisture distribution and governing accelerated failure processes initiating from the slope toe. In the realm of hydro-mechanical coupling processes and stability quantification, investigations have focused on fluid-solid interactions and stability evolution. Fan et al.¹⁹ quantified stability evolution under extreme rainfall conditions, revealing accelerated strength degradation triggered by hydro-mechanical coupling upon exceeding the plastic limit moisture content. Liu et al.²⁰ demonstrated how rainfall infiltration drastically reduces stability through rapid pore water pressure increase and matric suction elimination, triggering a progressive “push-pull” failure mechanism. Sasahara and Sakai²¹ monitored the dynamic coupling variations of shear stress, volumetric water content, and pore water pressure during rainfall infiltration. Shi et al.²² revealed that intense rainfall induces progressive shallow flow-slide instability through soil softening, matric suction loss, and pore pressure elevation. Duan et al.²³ incorporated creep effects into a constitutive model, demonstrating significant increases in potential slip surface depth coupled with marked safety factor reduction due to rainfall-induced matric suction loss. Pertaining to soil property degradation and early-warning indicators, research has addressed rainfall-induced alterations in soil properties and the development of monitoring frameworks. Liu et al.²⁴ identified permeability coefficient reductions exceeding 68% coupled with significant shear strength degradation due to rainfall/irrigation. Chae et al.²⁵ proposed a volumetric water content gradient threshold for landslide early warning, though neglecting pore pressure evolution. Zhou et al.²⁶ systematically elucidated disaster mechanisms under extreme rainfall conditions and subsequently developed regional rainfall threshold models for early warning purposes. Existing studies generally lack in-depth investigation into the structural evolution and water migration mechanism of loess under rainfall conditions, and the coupled analysis of multiple factors is insufficient, and the hydrological-mechanical process is disjointed. In addition, there is still an obvious gap in the research on the dynamic process of the damage mode conversion, the field scale effect, and the long-term evolution law.

Aiming at the deficiencies of existing studies, this study takes the landslide of Shixiakou in Lanzhou, China, as the engineering background, and systematically analyzes the infiltration characteristics, matrix suction changes, pore water pressure response and crack extension law of the slope under rainfall conditions by constructing a 1:50 scale loess slope model, simulating the natural rainfall process, and combining with the distributed sensor monitoring technology. Specifically, the study innovatively adopts real-time soil moisture dynamics, pore water pressure changes, and lateral stress distribution to reveal the dynamic evolution mechanism of rainfall-induced loess slope instability. Emphasizing the key role of cracks as a preferred channel for water infiltration, the study summarizes a four-stage progressive damage process: initial surface scour, foot of slope instability, mid-slope shear damage, and eventual collapse of the top section of the slope. To provide an experimental basis for establishing a refined landslide early warning index system, this study further proposes engineering prevention and control measures in the design, construction, and operation stages, which are of great theoretical significance and engineering application value to enhance the ability of slope disaster prevention and control in loess areas.

Experimental design and operating conditions

Geological prototype

The Jiuzhou Shixiakou landslide in the Chengguan District of Lanzhou City is located in the V-level high-order area of the Yellow River. The terrain is relatively high, sloping from the northwest to the southeast. The elevation ranges from 1,540 to 1,700 m, with a relative relief of 100–150 m. Due to the damage caused by water erosion and man-made transformation in the later stage, the terrace morphology is no longer obvious, and the total height of the mountain is 140 m. The landslide plane is fan-shaped, the length of the landslide is 75 m, the width of the trailing edge is 25 m, the width of the leading edge is 95 m, and the slope is 45 ~ 63 °. The slope surface is steep and gentle, and the rest of the slope has lost the basic form of the original river terrace landform due to rainfall erosion, as shown in Fig. 1. The exposed stratigraphy of the landslide area is relatively simple, ranging from youngest to oldest as follows: Holocene landslide deposits (Q4) are mainly distributed in the middle of the landslide body and its frontal area, with lithology consisting predominantly of reworked material from fragmented Malan Loess and Gaolan Group shale; Pleistocene (Q3) unit is represented by the more extensively distributed Malan Loess, which drapes over the older strata; In the middle Pleistocene, there are sporadic exposures on both sides of the gully and the lower part of the steep wall in front of the slope, which can be divided into two phases. Early accumulations of alluvial deposits and late accumulations of wind-deposited alluvial loess. The lower part is mainly distributed in the Cretaceous sandstone.

Meteorological conditions

The unstable slopes of the Jiuzhou district are located at the northern edge of the inland temperate semi-arid climate zone, and their meteorological conditions are characterised by significant spatial and temporal variability.

The Fig. 2 presents the long-term observational data from the meteorological station in Chengguan District, Lanzhou City. The average annual precipitation in the region is 311.7 mm. Precipitation exhibits a typical single-peak distribution throughout the year, with the main flood season occurring from July to September. This period accounts for over 60% of the total annual precipitation. The inter-annual fluctuation is characterised by a short cycle of 4 years and a long cycle of 8–11 years, with a maximum precipitation of 423.5 mm and a minimum of 189.2 mm in the year of extreme values. It is worth noting that the difference in precipitation extremes in August

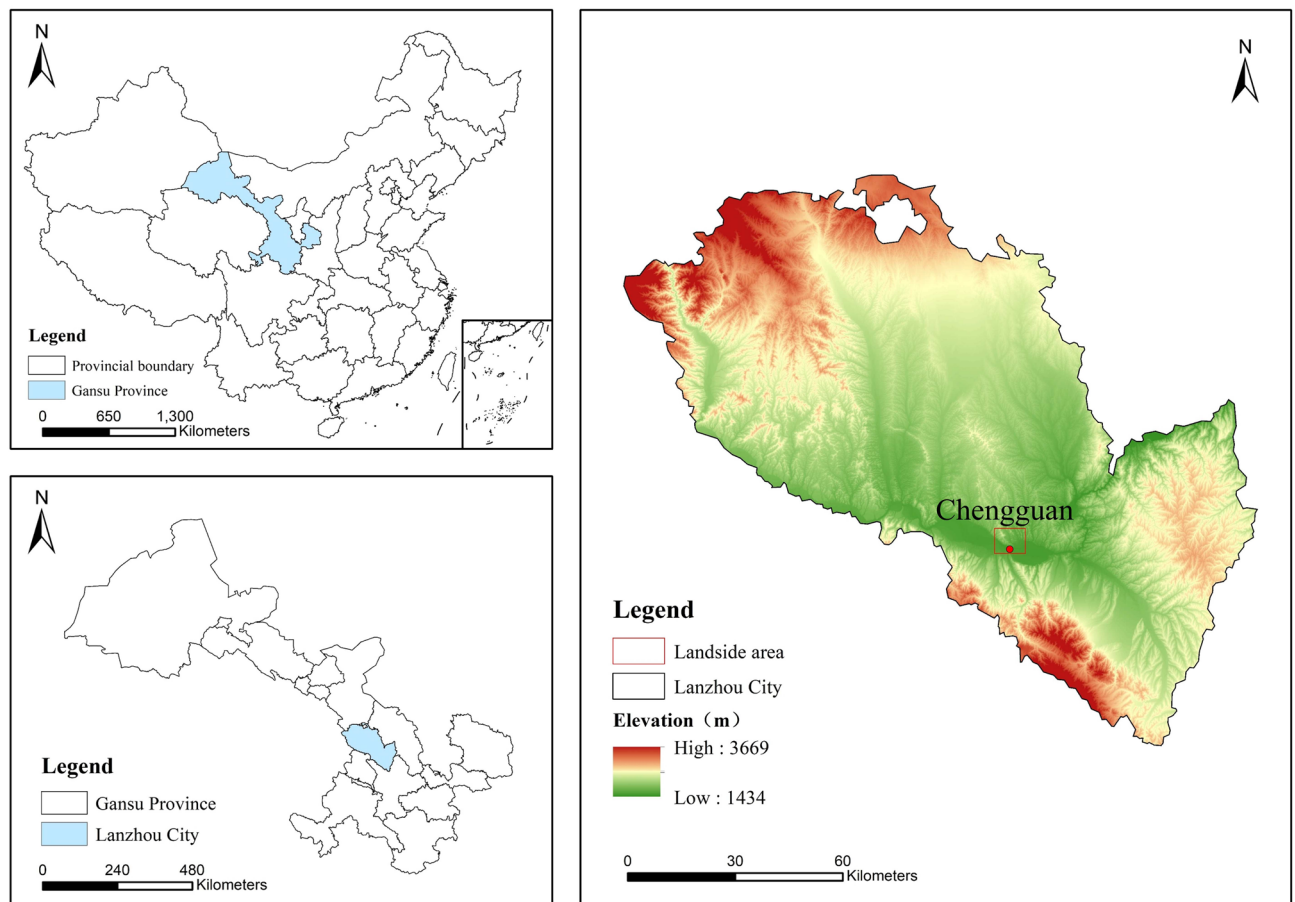


Fig. 1. Location map of Shixiakou landslide, Chengguan District, Lanzhou City, China. The elevation data were obtained from the Geospatial Data Cloud (<http://www.gscloud.cn/>). The administrative division data were sourced from the National Platform for Common Geospatial Information Services (<https://www.tianditu.gov.cn/>). The map was generated and post-processed using ArcGIS software (version 10.5; Esri, <https://www.esri.com/>).

is significant, with a maximum daily rainfall of 96.8 mm, a maximum hourly rainfall of 68 mm, and a maximum rainfall of 18.6 mm in 10 min. In addition, there is a record of 9 consecutive days of persistent rainfall in the region, with a cumulative rainfall of 168.3 mm. The superposition of such high-intensity, short-duration extreme precipitation events and persistent rainfall constitutes a unique rainfall feature in the region, which poses a significant threat to slope stability.

Test materials

The loess taken for the experimental materials was taken from the loess slope at the mouth of the Jiuzhou Gorge. To guarantee the consistency between the natural loess slope and the experimental fill slope, comprehensive laboratory analyses were conducted on Malan loess to characterize its physical and hydraulic parameters. The sampling locations are shown in Fig. 3. These analyses encompassed determinations of specific gravity, saturation moisture content, shear strength parameters through direct shear testing, compressibility characteristics via consolidation testing, and in-situ density measurements. Three samples were used in each test. The results of the tests are given in Table 1. Experimental results revealed a peak dry density of 1.64 g/cm³ and an optimal moisture content of 17.425%. To investigate the failure process of loess embankments during precipitation events, conventional triaxial shear tests under unconsolidated-undrained conditions were conducted to evaluate the strength characteristics of compacted Malan loess at varying saturation levels. The cylindrical specimens, measuring 39.8 mm in diameter and 80 mm in height, were prepared at maximum dry density. A series of tests was performed under confining pressures of 100, 200, and 300 kPa for samples with volumetric water contents of 10%, 15%, 20%, and 25%. As demonstrated in Table 2, both cohesion and internal friction angle exhibited water content-dependent reduction, with cohesive strength demonstrating more pronounced deterioration compared to frictional resistance. This moisture-induced strength degradation mechanism explains how rainfall infiltration critically compromises loess slope stability through shear strength reduction.

Figure 4 illustrates the variation of shear strength parameters with water content, as derived from fitting the results of triaxial tests conducted under different confining pressures. Both the cohesion and the internal friction angle decrease significantly with increasing volumetric water content. When the water content rises

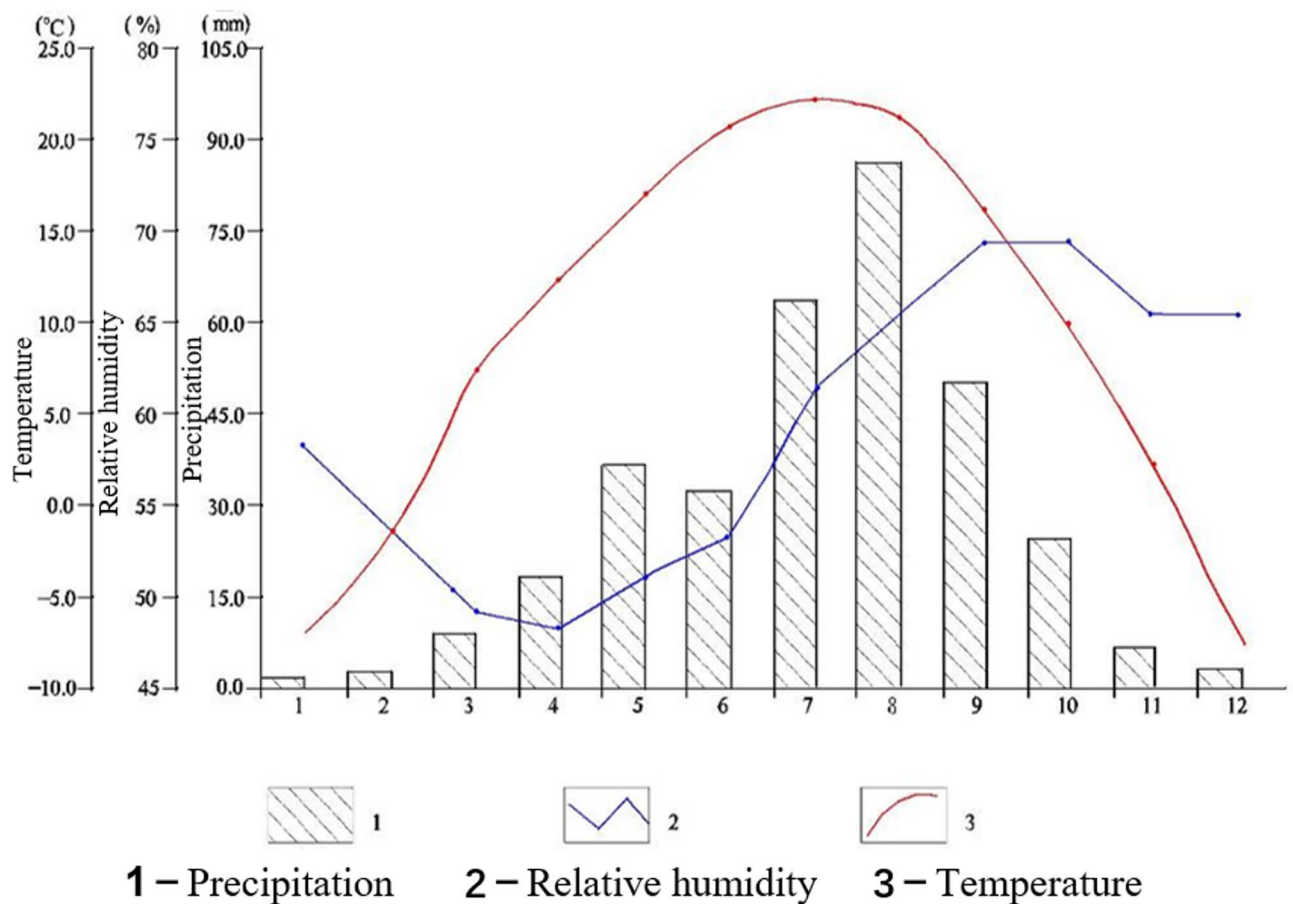


Fig. 2. Lanzhou meteorological elements map.

from 10% to 25%, the cohesion decreases by approximately 31.7%, and the internal friction angle decreases by approximately 56.3%. This indicates that water has a pronounced lubricating and softening effect on the loess, with a particularly severe impact on the frictional characteristics between soil particles. This core hydro-mechanical coupling relationship forms the fundamental basis for the subsequent analysis of the progressive instability of the slope induced by rainfall infiltration.

Loess test slope

The loess slope in this experiment is designed based on the actual loess slopes in the research. The selection of proper slope model dimensions is crucial as it significantly influences experimental accuracy. Excessively small models may yield unobservable results, while oversized models would substantially increase research costs. This physical model test was designed as a mechanism-focused model. The primary objective was to qualitatively investigate key failure processes in loess slopes under extreme rainfall, rather than to achieve complete similarity in all physical quantities.

According to the overview of the Jiuzhou landslide described in article 2.1, the slope length of the landslide is 75 m, and the slope angle ranges from 45° to 63°. By comprehensively considering the width data of the landslide rear edge and the landslide front edge, and based on the similarity theory and previous research results, the slope length of the test model is set to 1.5 m after conversion according to the slope scale of 1:50. This configuration resulted in a geometric scale of approximately 1:50 relative to the prototype Shixiakou landslide (length ~ 75 m, height ~ 60 m), determined by the prototype dimensions and laboratory constraints. For safety considerations, the slope angle of the test model is finally determined to be 45°. In addition, to reduce the influence of boundary effects, the height, width, and length of the slope body are set to 1.4 m, 1.45 m, and 2 m, respectively, to ensure that the slope length is close to the design requirement of 1.5 m. The model container's sidewalls were coated with Vaseline to reduce interfacial friction between the walls and loess material. Figure 5 illustrates the constructed loess test slope configuration.

To achieve an accurate simulation of natural loess slope conditions in laboratory settings, the experimental setup employed undisturbed loess material for constructing the foundational layer beneath the test slope. This foundation layer was precisely prepared with a height of 30 cm and compacted to achieve 100% density, ensuring complete consistency with the physical properties of the original undisturbed soil samples. Special attention was given to the interface treatment between the base and the experimental slope, where surface roughening

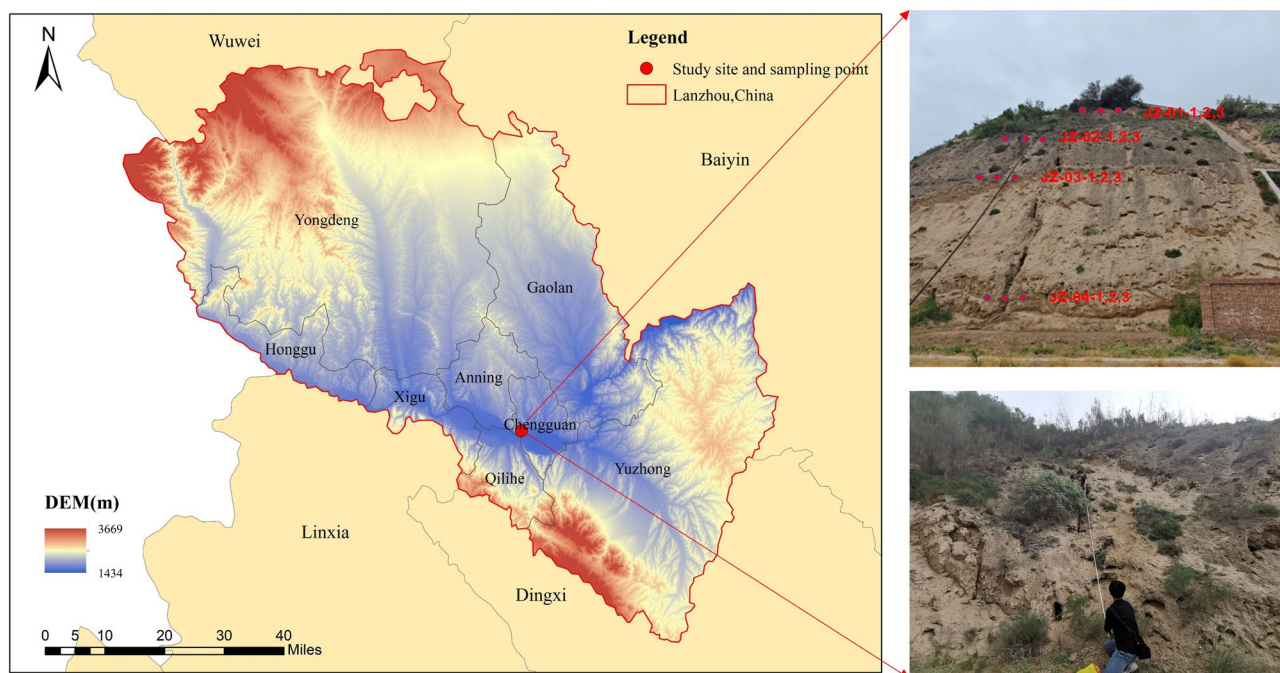


Fig. 3. Ketch map of sampling locations. The elevation data were obtained from the Geospatial Data Cloud (<http://www.gscloud.cn/>). The administrative division data were sourced from the National Platform for Common Geospatial Information Services (<https://www.tianditu.gov.cn/>). The map was generated and post-processed using ArcGIS software (version 10.5; Esri, <https://www.esri.com/>).

Proportion (g·cm ⁻³)	Natural moisture content ω/%	Optimal moisture content ω/%	Maximum dry density (g·cm ⁻³)	Liquid limit ω _L /%	Plastic limit ω _P /%
2.6997	11.811	17.425	1.6422	29.039	17.571

Table 1. Basic physical properties of soil samples.

Confining pressure /kPa	Volumetric water content ω/%	Shear strength parameter	
		c(kPa)	φ(°)
	10	29.97	30.34
	15	27.77	30.34
100, 200, 300	20	24.65	19.34
	25	20.46	13.25

Table 2. Shear strength parameters of Malan loess under different volumetric water contents.

techniques were applied to effectively mitigate potential boundary effects that could compromise experimental validity.

The construction methodology employed a carefully designed triangular support structure to facilitate the layered filling process of the test slope. Each fill layer was controlled at a uniform thickness of 0.3 m, with the surface meticulously monitored and adjusted using a combination of infrared laser technology and precision leveling instruments. As clearly illustrated in Fig. 6, the achieved compaction characteristics of the constructed slope precisely matched those observed in natural loess formations. The initial moisture conditions of the test slope were maintained within a narrow range of 11.6% to 12.09% volumetric water content, while maintaining a consistent 1:1 slope gradient throughout the construction process.

Quality assurance measures included comprehensive uniformity verification through systematic sampling at five strategically selected locations using a standardized ring sampler with dimensions of 61.8 mm in diameter and 20.0 mm in height (as documented in Fig. 7). These samples enabled precise measurement and verification of compaction characteristics for each layer. Notably, the compaction process for the model slope involved enhanced techniques that resulted in greater density compared to natural slope conditions, particularly due

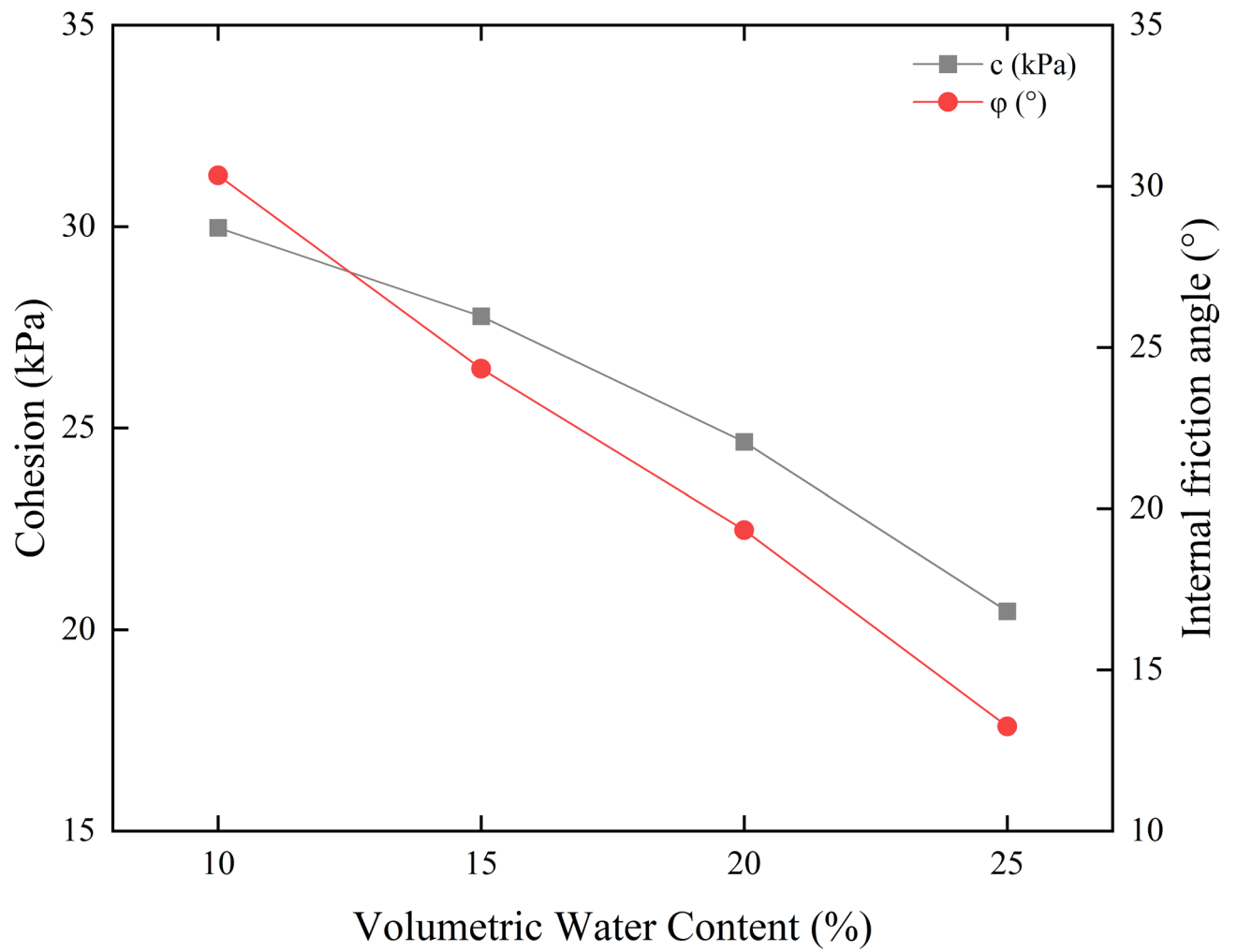


Fig. 4. Shear strength parameters versus water content.



Fig. 5. Loess test slope.



Fig. 6. Test loess filling to determine its horizontal.

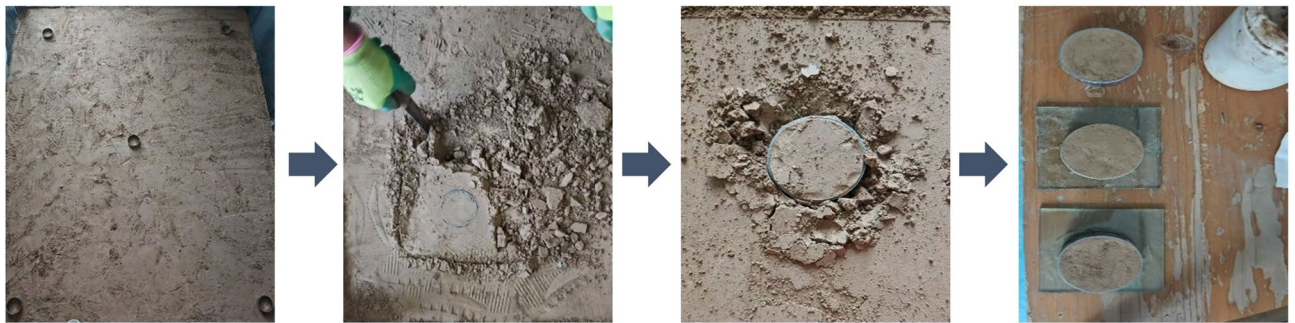


Fig. 7. The sampling process of the loess filling and breaking ring knife.

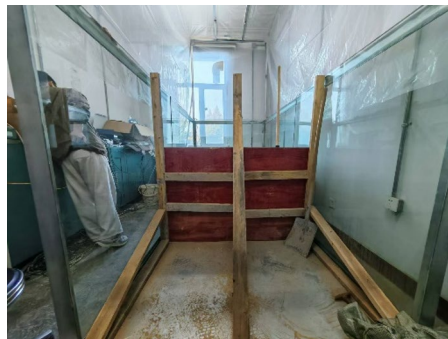


Fig. 8. Test loess filling slope diagram.

to the reduced scale of the experimental prototype. This density differential was carefully evaluated through repeated comparative analyses.

The experimental setup incorporated a systematic monitoring network with designated measurement stations labeled as downhill, mid-slope, and uphill positions, each spaced at consistent 0.25-meter intervals along the slope profile. Following completion of construction, the experimental slope underwent a carefully controlled one-week curing period to allow for proper stabilization before testing commenced. The complete construction sequence and methodology are visually documented in Fig. 8, providing a comprehensive reference for experimental replication.

Test device

The experimental investigation utilized a specially fabricated steel model tank with dimensions of 3.0 m (length) × 1.5 m (width) × 1.5 m (height) to accommodate the loess fill slope. The tank's sidewalls were constructed with 1.6 cm-thick reinforced glass panels, which were marked with a 10 × 10 cm grid system to enable precise

observation of rainwater infiltration patterns and slope deformation processes. While the back and bottom surfaces of the tank were sealed with steel plates to prevent water leakage, the front and top remained open to facilitate observation and rainfall application. A custom-designed rainfall simulation system was installed above the tank, consisting of a water storage tank, high-pressure pump (maintained at 0.5 MPa), distribution piping network, fine mist nozzles, pressure gauge, and flow meter. To ensure the rationality of the stress state in the model, the initial stress condition of the slope was evaluated before testing. Based on the model geometry (height = 1.4 m) and the natural unit weight of the loess ($14.7 \text{ kN}\cdot\text{m}^{-3}$), the theoretical self-weight stress at the slope toe is approximately 20.6 kPa. The initial horizontal earth pressures measured by the embedded sensors prior to rainfall ranged between 0.5 and 2.0 kPa, which is significantly lower than the theoretical self-weight stress. This discrepancy is primarily attributed to the boundary constraints of the model container (e.g., sidewall lubrication, rigid container walls) and potential stress release during sensor installation. Nevertheless, this study focuses on trends in stress variation and their coupling with hydrological responses rather than absolute values. Therefore, the measured initial stress state remains valid for revealing the dynamic stress redistribution process during rainfall infiltration. The rainfall intensity was set by adjusting the system pressure and valve opening, and was monitored in real-time via the flow meter. To achieve the target intensity of 73.5 mm/h, the system was calibrated before the test: under a stable pressure (0.5 MPa), the flow meter reading was converted based on the rainfall-receiving area of the model box ($3.0 \text{ m} \times 1.5 \text{ m}$), and the valve was finely adjusted until the predetermined intensity was attained. To ensure spatial uniformity of rainfall distribution, the 10 atomizing nozzles were arranged linearly at a height of 1.0 m above the model box with a spacing of 0.5 m. The simulated rainfall infiltrated vertically through the slope profile, with excess water draining from the open front section. An array of monitoring instruments, including volumetric water content sensors, pore water pressure transducers, and horizontal earth pressure cells, was strategically embedded at various depths within the loess slope to capture the hydrological and mechanical responses during testing. The complete experimental setup, illustrating the integrated systems for controlled rainfall application and multi-parameter monitoring, is presented in Fig. 9, demonstrating the comprehensive approach adopted to investigate rainfall-induced slope.

Figure 10 presents the sensor layout in plan and profile views. Monitoring devices were installed during slope construction, with specifications listed in Table 3. All sensors were calibrated and connected to data loggers before testing. Three cameras (left, front, rear) recorded the experiment.

In recent years, short-term heavy rainfall events have occurred frequently in Gansu. Studies have shown that the hourly rainfall intensity in central Gansu can be as high as 60–80 mm, which echoes the meteorological conditions in the Jiuzhou area described in 2.2, and together reveal a significant increase in extreme precipitation under the influence of climate variability. According to the official meteorological data released in July 2023, the maximum hourly rainfall intensity in Gansu Province has reached 73.5 mm. By comparing this data with the previous loess slope model test conditions in the region, it is clear that the current extreme rainfall situation has changed significantly.

To realistically simulate the impact of such extreme rainfall on loess slopes, this experiment employed a rainfall intensity of 73.5 mm/h. The selected intensity corresponds to recent records of short-duration extreme rainfall in the Lanzhou region (Sect. 2.2). In geotechnical physical models focused on infiltration and failure

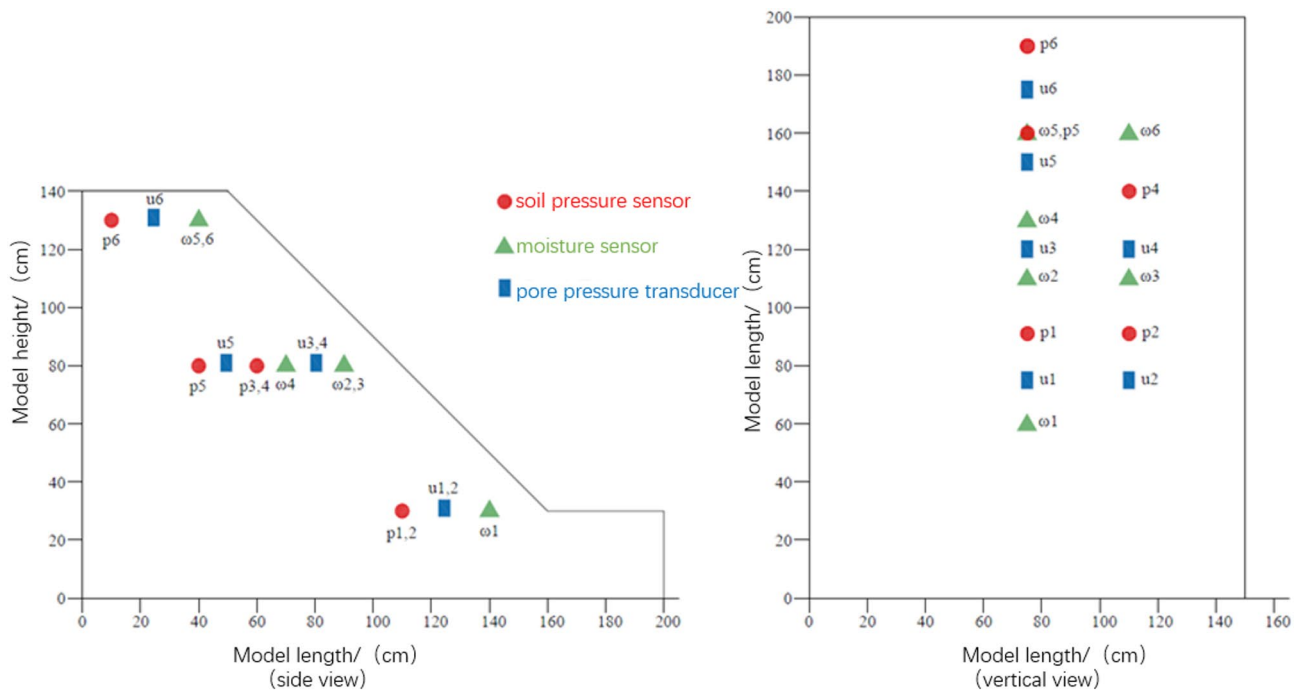


Fig. 9. Test device layout.

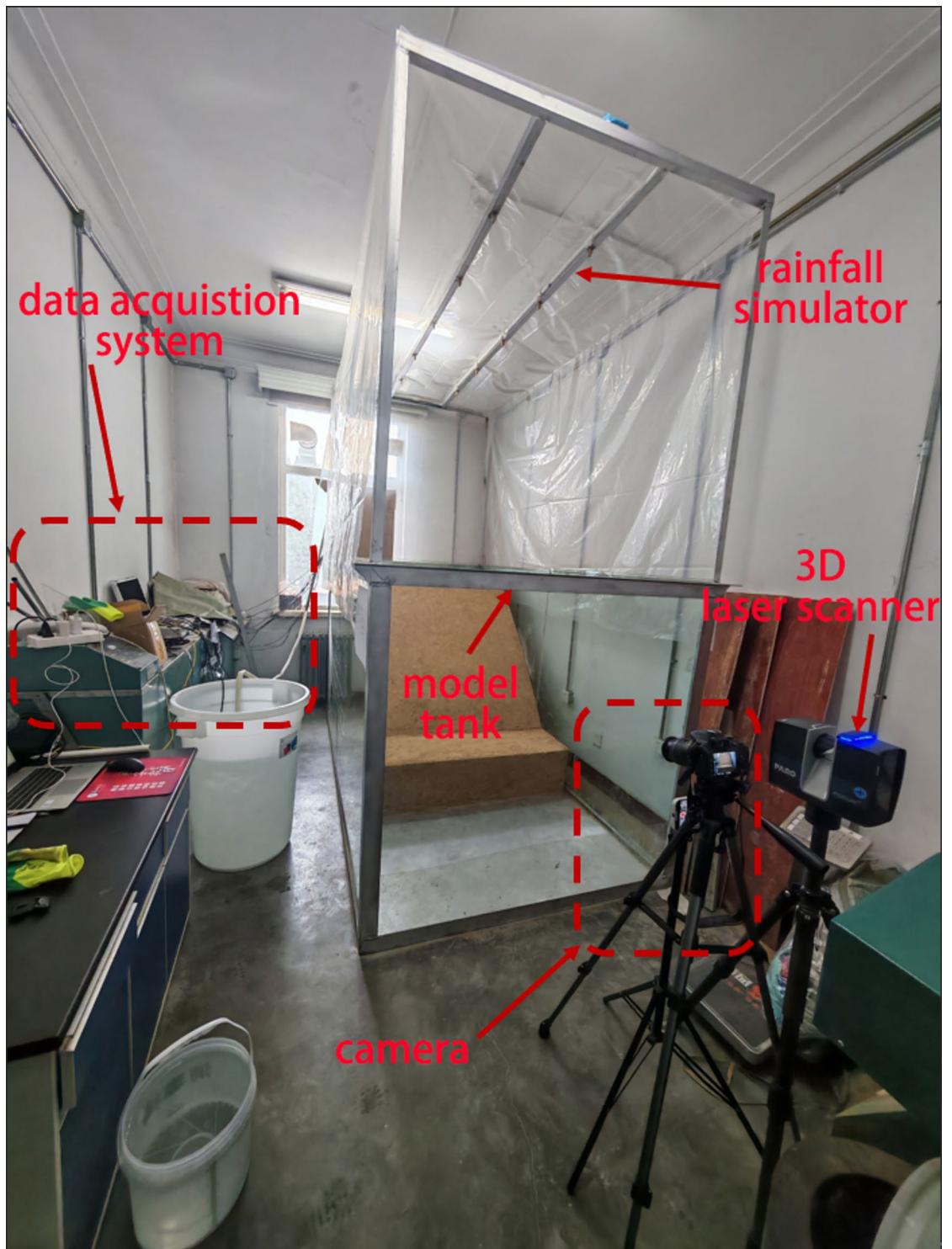


Fig. 10. Monitoring device layout diagram.

mechanisms, a widely accepted simplification is to apply the same rainfall intensity as in the field prototype²⁷ (i.e., a 1:1 scaling ratio). This approach preserves the fundamental competition between rainfall supply and soil infiltration capacity, which is crucial for realistically triggering key instability processes such as surface runoff and internal pore-pressure generation. The simulated rainfall thus represents an intensified scenario to accelerate the failure progression for clear observation. The rainfall lasted for a duration of 14 h, starting at 8:00 a.m., with the rainfall pattern illustrated in Fig. 11. The simulated rainfall was driven by a pressurized water system, where rainfall intensity is regulated by adjusting the water pressure—higher pressure yields greater

Name and model	Type	Precision	Range
DMTY micro soil pressure cell	vibration wire	0.1 kPa	800 ~ 1500 $\mu\text{ε}/\text{kg}/\text{cm}^2$
Soil moisture sensor	resistive	$\pm 2\%$	0–1
DMKY micro pore water pressure gauge	voltage way	0.2%	-10 ~ 20 kPa
DMYB series of dynamic and static strain acquisition instruments	vibration wire	0.1 Hz	0 ~ 6000 Hz

Table 3. Statistical table of test monitoring instruments.

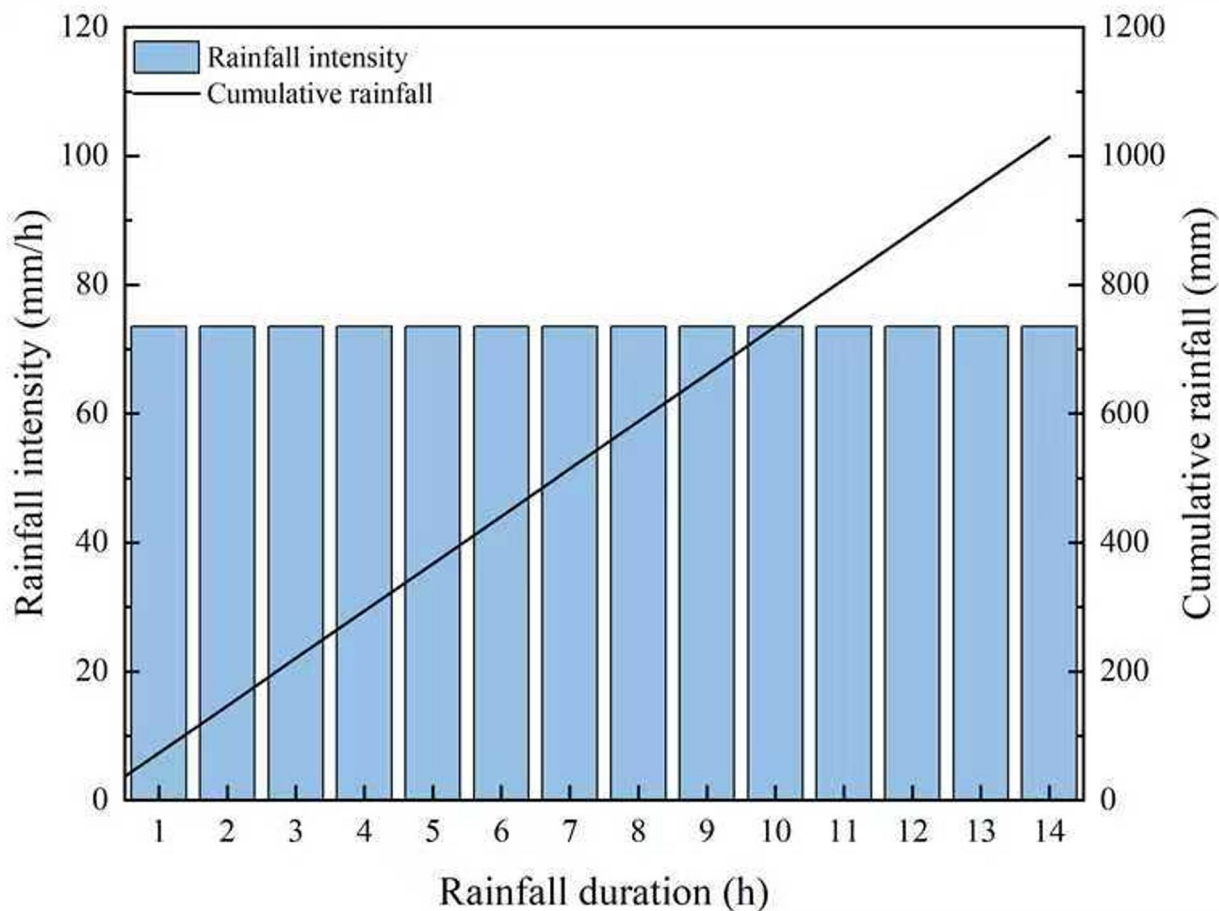


Fig. 11. Graph of rainfall relationship in model test.

intensity. In this study, by maintaining a constant water pressure of 0.5 MPa, a steady rainfall intensity of 73.5 mm/h was achieved.

Analysis of failure mechanism of loess fill slope Parameters change with rainfall

Figure 12 illustrates the temporal variations in volumetric water content at different monitoring points within a loess slope during rainfall infiltration, revealing two distinct hydrological response patterns attributable to differences in slope structure.

At the slope crest, monitoring point ω_6 exhibits an immediate response to the wetting front, with moisture content rapidly increasing to near saturation 26.8% and then stabilizing. This reflects the direct infiltration pathways and strong water retention capacity characteristic of the crest area. In the mid-slope section, which includes points ω_2 , ω_3 , and ω_4 , a gradual response pattern is observed. Both ω_2 and ω_3 reach peak saturation relatively quickly, undergo partial drainage, and eventually stabilize at a lower moisture level. Notably, although ω_2 and ω_4 are situated at the same depth, the arrival time of the wetting front differs significantly—63 min for ω_2 compared to 300 min for ω_4 . This delay is attributed to localized subsidence in the mid-slope region, which diverts preferential flow away from ω_4 , resulting in a lower maximum saturation of about 24.5%. Additionally, a sudden increase in moisture content at ω_4 after 130 min is likely associated with the development of micro-

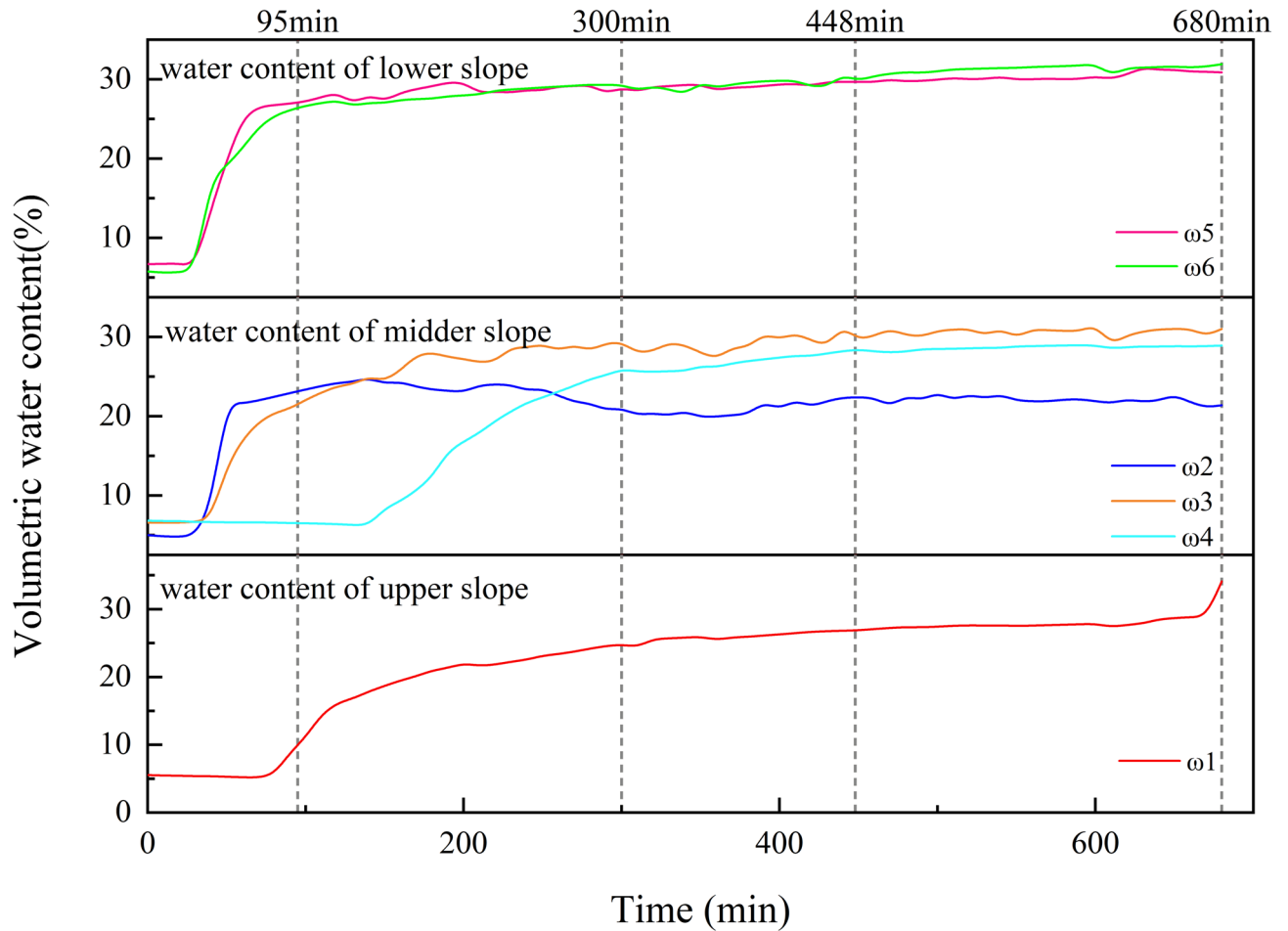


Fig. 12. Temporal variations of volumetric water content at different locations during rainfall infiltration.

fractures induced by gravitational forces and water infiltration. These fractures enhance local permeability and facilitate accelerated seepage. At the slope toe, monitoring point ω_1 shows a gradual hydrological response: moisture content increases slowly, attains a moderate saturation level, and subsequently changes only minimally. This behavior indicates a slower infiltration and redistribution process in the toe region, consistent with its more delayed reaction to rainfall infiltration.

The spatial and temporal differences in volumetric water content across the slope clearly demonstrate the development of preferential flow paths within the loess slope. The heterogeneity in moisture distribution, particularly the formation of these preferential pathways, directly influences the heterogeneous deformation behavior and failure mechanisms of loess fill slopes under rainfall conditions, underscoring the critical role of local structural variations in overall slope stability.

Figure 13 illustrates the pore water pressure variations in different sections of the experimental slope before failure. The piezometer u6 at the upper slope exhibited the most rapid response, which can be attributed to the increase in hydrostatic pressure caused by rainwater accumulation at the slope crest.

Overall, the evolution of pore water pressure displayed a three-stage pattern: an initial gradual rise as the wetting front reached each monitoring point, followed by significant fluctuations during the phase of accelerated slope deformation, and finally a continuous decline upon the onset of instability. It is noteworthy that the amplitude of pore water pressure changes in the middle and toe sections was considerably greater than that in the upper slope, indicating that these regions were subjected to more pronounced stress concentration during the deformation process.

Figure 14 illustrates the evolution of horizontal earth pressure in the slope during rainfall infiltration. Compared to volumetric water content and pore water pressure, the earth pressure responded more rapidly to rainfall, indicating the immediate influence of infiltrating water on the redistribution of gravitational stress. During the initial stage 0–95 min, the variation trends of earth pressure at all monitoring points were consistent. With continued rainfall and water accumulation at the slope crest, the horizontal earth pressure peaked at approximately 530 min, then gradually decreased as the wetting front propagated downward. Detailed analysis of the mid-slope sensor p4 revealed a close correlation between its pressure variation and moisture movement as well as local deformation: the initial increase corresponded to the rise in volumetric water content at ω_3 , followed by fluctuations around 2.35 kPa influenced by changes in pore water pressure at u4 and mid-slope

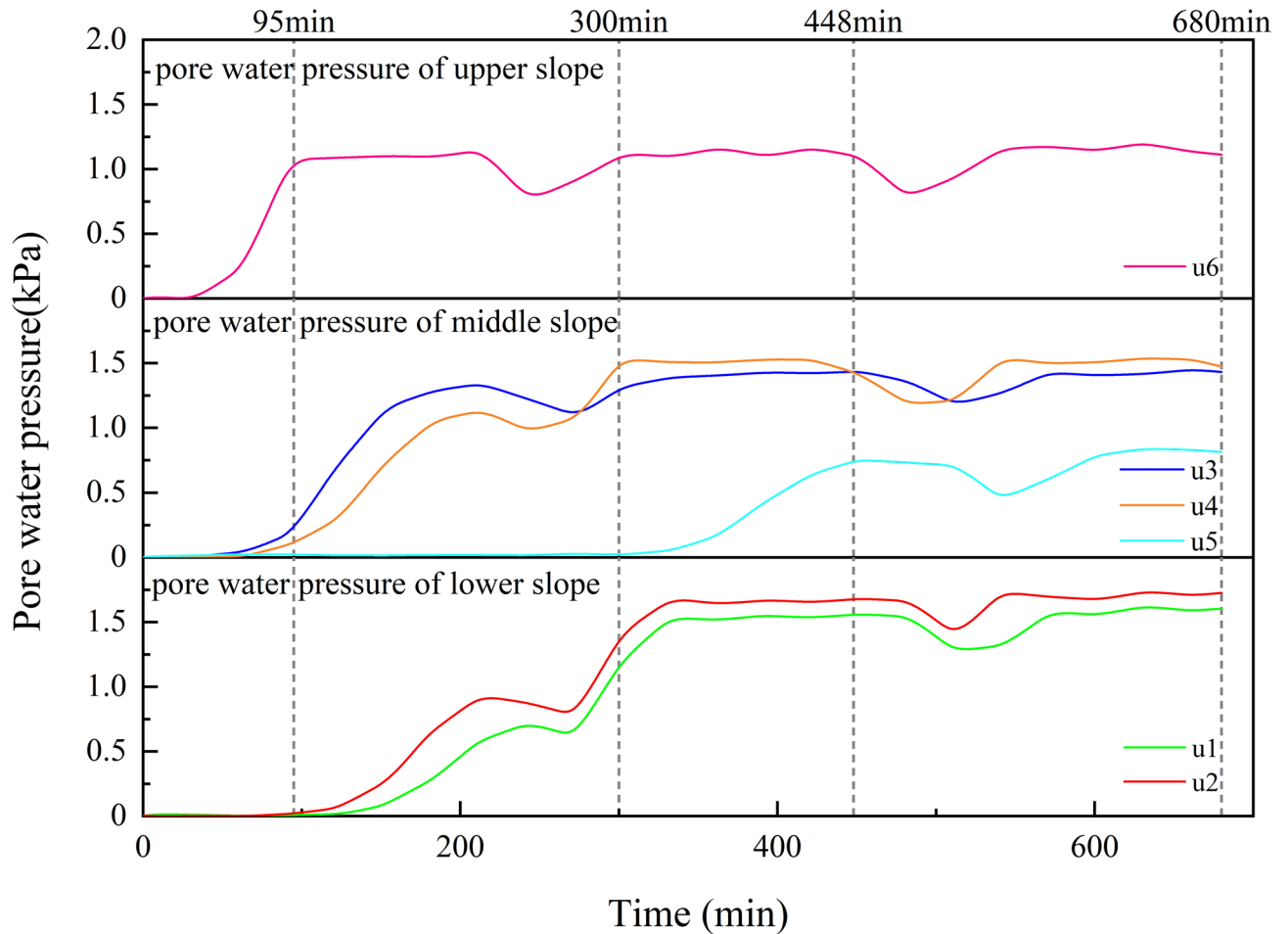


Fig. 13. Three-stage evolution of pore water pressure prior to slope failure.

deformation, culminating in an abrupt decrease during slope failure. Additionally, significant fluctuations were recorded by the upper-slope sensor p5 between 530 and 680 min, showing a high consistency with the variations observed at the mid-slope sensor p3.

The experimental results highlight two key findings: First, the notable pressure increment observed at p4 during slope failure indicates that horizontal stress concentration plays a critical role in the instability mechanism. Second, the amplitude of earth pressure variation in the slope crest was substantially greater than that in the middle and lower sections, underscoring the controlling influence of the crest on overall slope stability. These response patterns reflect the development of compression zones and stress concentration areas during soil deformation, providing important insights into the stress transfer mechanisms in rainfall-induced failures of loess slopes.

Failure mechanism analysis

Figure 15 illustrates the failure phenomenon of the physical model. The failure process can be divided into initial surface scouring, subsequent basal slope instability, progressive mid-slope shear failure, and ultimate crown section collapse four distinct stages. The field investigation conducted by Mu et al.²⁸ on the natural loess landslide at Shixiakou, clearly concluded that the Shixiakou landslide is a typical retrogressive landslide. Its instability initiates from the slope toe region, with rainfall infiltration and the vertical fissures developed in the loess—which provide rapid pathways for rainwater—identified as the primary triggering factors. These findings are highly consistent with the failure initiation location, progression sequence, and the controlling mechanism of fissure-accelerated seepage revealed in the model test of this study. Figure 16 shows the wetting front migration at different times, and Fig. 17 provides a schematic diagram of the corresponding process. Based on the monitoring data of volumetric water content, pore water pressure, and horizontal earth pressure during the rainfall process, this chapter systematically analyzes and discusses the failure mechanism of the loess slope.

Gully erosion and partial destruction stage

Initial surface scouring (0–95 min) Based on multi-temporal wetting front observations through the glass sidewall, the recorded migration rates of the wetting front at monitoring sensors in Sects. 1-1 range from 2.383 to 4.162 mm/min, with a mean value of 3.343 mm/min. Comparative analysis of rainfall infiltration rates at

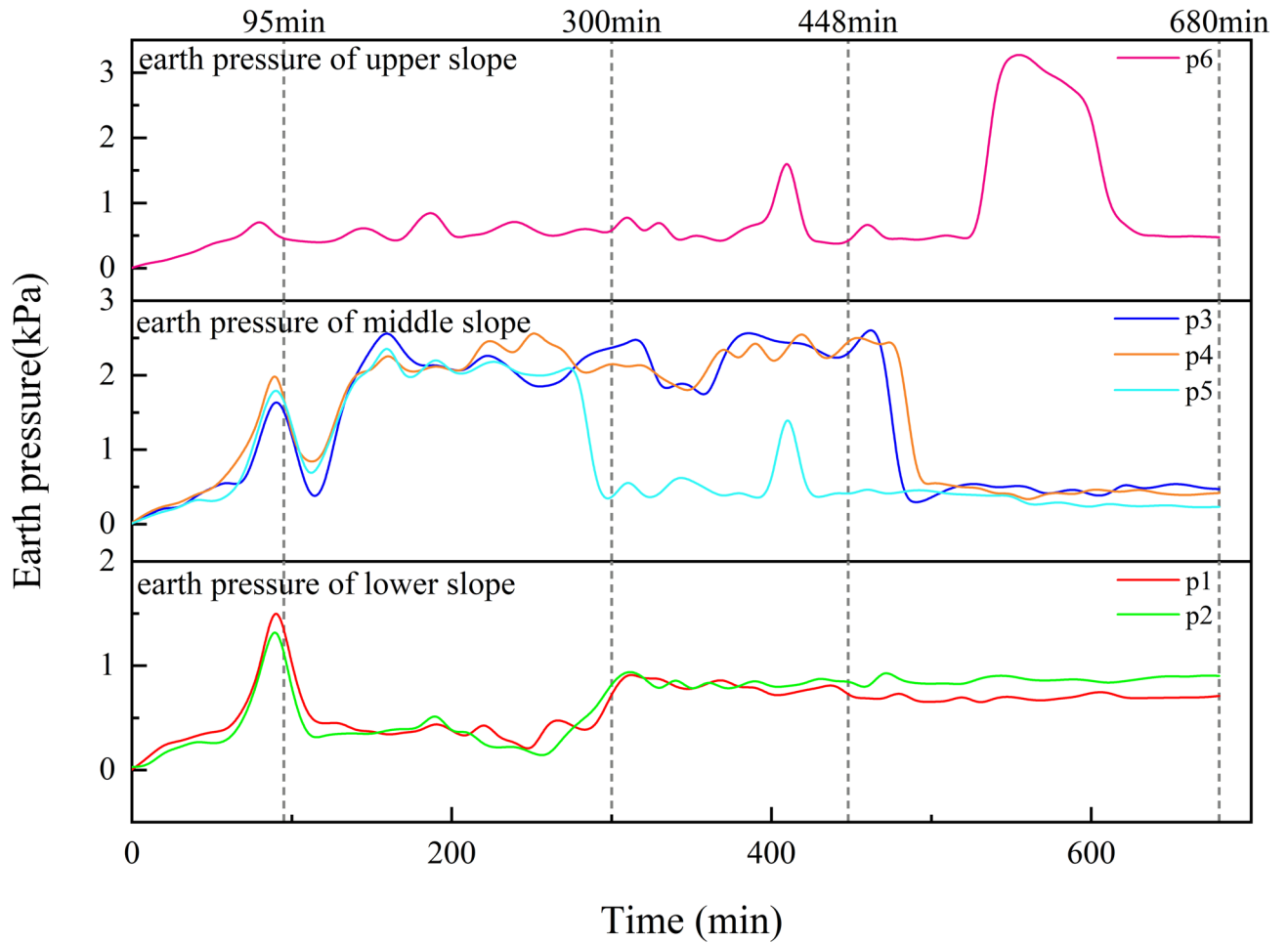


Fig. 14. Evolution of horizontal earth pressure during rainfall infiltration.

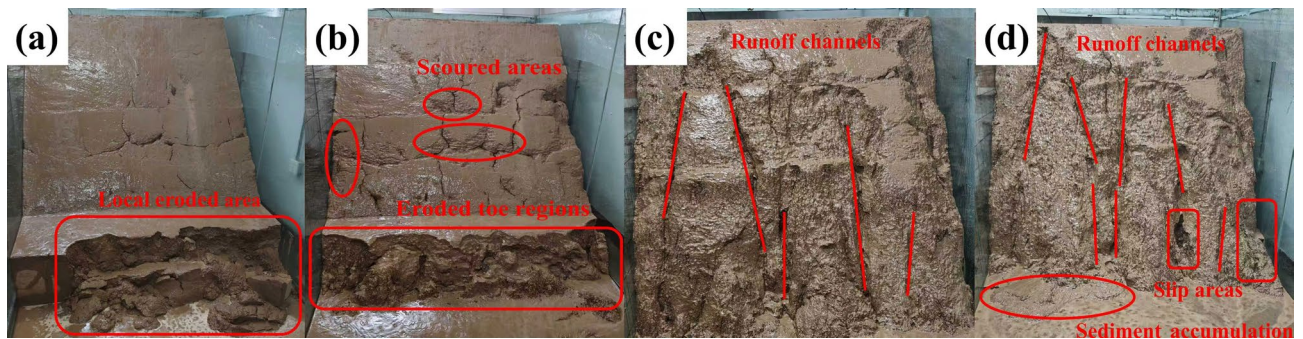


Fig. 15. Failure phenomena in physical model tests.

measuring points ω_1 , ω_3 , and ω_5 reveals a decreasing trend in infiltration capacity from the upper to the lower part of the slope. Specifically, the highest infiltration rate occurs in the embankment area, followed by the slope surface, while the lowest is observed in the mid-lower slope region.

In terms of spatial erosion characteristics, the most severe damage is identified at the toe of the slope, with moderate erosion occurring in the mid-slope section. This distribution is closely associated with the relatively slow migration of the wetting front along the slope, which restricts rainwater infiltration and leads to predominant discharge via surface runoff, thereby accelerating the loss of surficial loess. Furthermore, the slope can be hydrologically divided into three distinct zones: the upper slope corresponds to a drainage area, the mid-slope to a runoff zone, and the lower slope to a recharge area. Runoff intensity is highest in the lower slope and decreases upward toward the upper slope. Under the influence of this hydrological pattern, gully systems initially

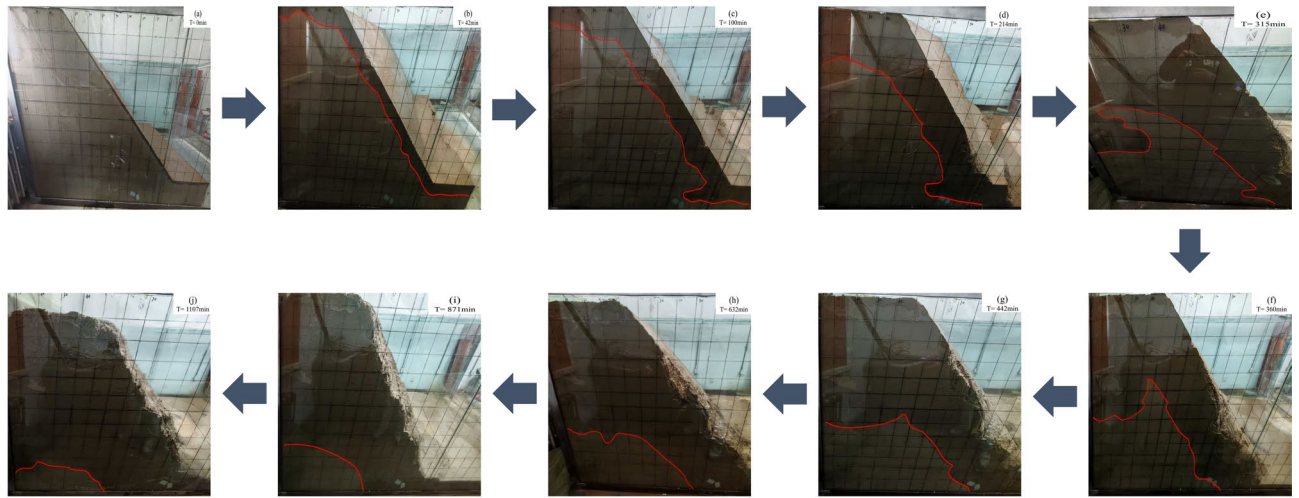


Fig. 16. Wetting front advancement at successive time points.

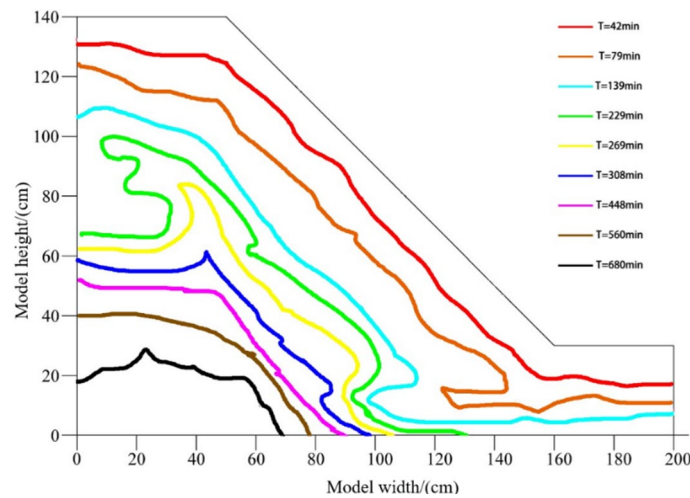


Fig. 17. Temporal evolution of the wetting front.

develop in gently sloped areas, which progressively evolve into preferred pathways for surface runoff, further intensifying the process of loess erosion.

Subsequent basal slope instability (95–300 min) Prolonged rainfall induced a coupled interaction between horizontal earth pressure and pore water pressure in the saturated zone, leading to localized slip and collapse failure. The failure mechanism stems from two primary factors. First, the unique pore structure and mineral composition of the loess resulted in differential settlement under continuous infiltration, triggering shear deformation, while the near-saturation of the superficial soil significantly reduced its shear strength. Second, as illustrated in Fig. 13, the accumulating gravitational load at the slope crest caused pore water pressure at monitoring points u5 and u6 in the locally disturbed zone to peak, further weakening the soil's shear resistance and promoting progressive displacement at the slope toe. Concurrently, the horizontal earth pressure at points p3 and p4 exhibited notable fluctuations and a continuous increase, as shown in Fig. 14, further compromising slope stability.

Monitoring data indicate that spatial heterogeneity in volumetric water content and surface erosion were the main contributors to slope toe failure. Figure 12 reveals significant variation in volumetric water content at the slope toe, where the value at ω_6 increased to 29.1%, indicating the presence of lateral seepage in the embankment area. This lateral flow enhances vertical infiltration capacity, accelerating the downward migration of moisture. Furthermore, Fig. 16 demonstrates higher permeability beneath the embankment compared to the slope surface, suggesting that a slip surface may have developed within the saturated zone near the slope toe. It is noteworthy that, as shown in Fig. 15, under the combined influence of overburden weight and pore water pressure, fissures initially formed at Retaining Fill I, providing preferential pathways for rainwater infiltration and ultimately leading to the failure of the slope toe.

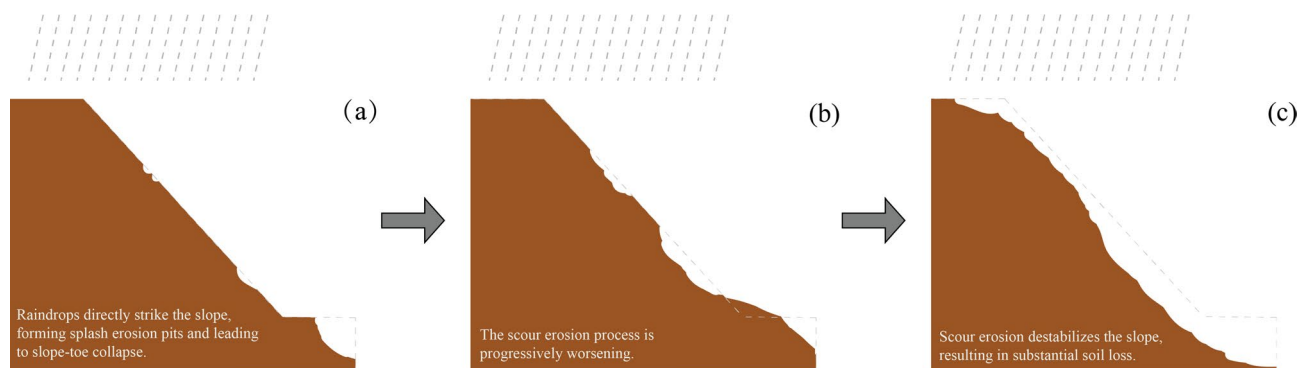


Fig. 18. Schematic diagram of the process of rainfall-induced slope erosion and failure.

Progressive mid-slope shear failure (300–448 min) When the cumulative rainfall reached 541.32 mm, the mid-slope region exhibited a significant increase in sliding velocity and a notably longer sliding distance. The loss of toe support due to localized collapse and slope foot instability led to substantial alterations in slope geometry, seepage pathways, and stress distribution. These changes promoted the formation of new seepage surfaces along potential sliding zones, resulting in excessive drainage—a phenomenon corroborated by synchronous variations in volumetric water content at monitoring points ω_1 and ω_4 . Concurrently, enhanced rainwater infiltration caused the volumetric water content at ω_3 to gradually rise to 30.3%, reflecting ongoing moisture redistribution within the slope.

The removal of toe support also induced stress concentration in the mid-slope section. As shown in Figs. 13 and 14, pore water pressure at points u3 and u4 displayed an increasing trend, while the horizontal earth pressure at p2 fluctuated around 0.42 kPa. Under these conditions, numerous tensile cracks developed in the central part of the slope, significantly exacerbating the overall damage to the slope structure. Therefore, a systematic understanding of fracture evolution is essential for elucidating the failure mechanism of loess slopes, which will be further discussed in subsequent sections.

Ultimate crown section collapse (448–680 min) Based on the failure morphology at the slope crest and monitoring data analysis, the slope failure at this stage was characterized by long sliding distance, limited scale, and rapid movement, with overall instability occurring when cumulative rainfall reached 1029 mm. As shown in Fig. 14, the instability in the slope crest area primarily resulted from stress concentration, which caused a sharp increase in horizontal earth pressure at point P3 and adjacent monitoring points to 0.4 kPa, indicating significant stress redistribution in this region. Meanwhile, the volumetric water content at various monitoring points on the slope crest remained relatively stable, suggesting limited direct influence of moisture migration on the failure at this stage. However, a notable decrease in pore water pressure at point p6 reflected altered drainage conditions or structural loosening of the soil prior to instability.

The observed failure pattern, featuring continuous tensile cracks and localized subsidence at the slope crest, further confirms brittle failure characteristics induced by stress concentration. This phenomenon indicates that under the combined effects of prolonged rainfall infiltration and gravitational stress, the tensile strength of the soil at the slope crest progressively weakened, ultimately leading to the formation of a continuous slip surface. This failure mechanism elucidates the key process by which loess slopes transition from local instability to overall sliding under high cumulative rainfall conditions.

Fracture evolution and erosion coupling mechanism

Under rainfall conditions, the coupling between fracture development and surface erosion constitutes a critical mechanism leading to instability in loess-filled slopes. Due to the protracted and insidious nature of these deformation processes, complete failure evolution is rarely systematically captured in field investigations. Through multi-source monitoring data encompassing volumetric water content, pore water pressure, earth pressure, and acceleration, this study elucidates the full progression from incipient microfracture development to macroscopic slope failure.

As depicted in Fig. 18a, the initial rainfall phase involves raindrop impact directly on the slope surface, generating splash erosion pits and triggering localized collapse at the slope toe. This process compromises the original slope structure, inducing differential settlement in the central slope region where initial microfractures develop. Under the coupled influence of differential settlement and rainwater infiltration, accumulated plastic deformation progresses to brittle fracture failure. The emerging fracture network not only disrupts soil continuity but also establishes preferential pathways for moisture migration.

During fracture propagation, controlled by spatial heterogeneity in soil strength and moisture distribution, fractures exhibit arcuate transverse expansion. Significantly, preferential flow networks develop within the slope prior to visible fracture formation. Concurrent intensification of surface scour erosion, illustrated in Fig. 18b, further degrades slope integrity and accelerates longitudinal fracture extension.

Progressive fracture development creates effective catchment zones behind the fractures, substantially enhancing rainwater accumulation. Moisture diffusion within fractures significantly reduces soil strength in the

fracture-tip zone, while accumulated water generates static pressure that persistently undermines slope stability. Monitoring data reveal pronounced fluctuations in pore water pressure and earth pressure during this phase, indicating fracture propagation to the slope toe and formation of potential slip boundaries.

The final instability stage involves interconnection between rear-edge fractures and leading-edge shear surfaces, forming a continuous slip plane as shown in Fig. 18c. Driven by rapid discharge of accumulated water behind the fractures, the slope undergoes rapid sliding accompanied by substantial soil loss. Crucially, unlike sand-clay slopes where failure is primarily governed by pore water pressure, loess slope instability represents a dynamic coupling process between fracture development and erosion mechanisms. This understanding provides a vital theoretical foundation for loess slope hazard mitigation.

Integrated engineering mitigation strategies

Based on systematic observations of failure modes and mechanisms across each degradation stage, integrated engineering prevention and control measures are proposed to effectively reduce landslide risks, with optimizations spanning the early design, construction, and operation phases.

Early design and construction stage

- (1) In view of the rainfall infiltration being the key factor leading to the destruction of the loess slope, it is suggested that the disposal ditch should be set up reasonably in the slope protection and slope surface of each slope. Through these disposal ditches, the rainwater flow direction can be effectively guided, the infiltration of rainwater into the slope can be significantly reduced, and the risk of slope damage caused by rainwater immersion can be reduced.
- (2) A suitable curing agent can be selected to reinforce the slope. The curing agent can react with the surface soil to enhance the cohesion between the soil particles, thereby improving the strength and anti-scouring ability of the surface soil, and effectively resisting the erosion of the slope by natural factors such as rainwater.
- (3) It is an effective measure to carry out deep vegetation protection on the slope. The roots of the vegetation can penetrate into the soil and play a role in anchoring the soil. At the same time, it can also reduce the runoff speed of the slope and reduce the degree of erosion. In addition, the transpiration of vegetation helps to reduce the pore water pressure in the soil, improve the shear strength of the soil, and enhance the stability of the slope.
- (4) The installation of surface grille soil nails on the slope can effectively restrain the deformation of the soil. When encountering rainfall infiltration, soil nails and grids can work together to share the stress borne by the soil, reduce the deformation of the loess slope due to rainfall, and enhance the stability of the loess slope under various working conditions.

Operation stage

- (1) During the operation phase, industrial and agricultural water should be channeled to the slope toe via specially designed drainage conduits. This approach prevents unregulated infiltration of water into the slope, mitigates soil strength degradation caused by excessive water penetration, and thereby safeguards slope stability.
- (2) Establishing a comprehensive monitoring system is critical for real-time tracking of slope deformation and hydrological variations. Upon identification of surface or embankment cracks, immediate backfilling measures must be implemented. Timely crack remediation effectively inhibits rainwater infiltration along fissures, averting a cascade of stability issues triggered by water seepage.
- (3) Given the progressive failure mode of loess slopes starting from the toe, mid-slope reinforcement (e.g., bolt anchoring and retaining wall support) should be promptly initiated upon toe damage. Concurrently, unstable toe regions require timely backfill reinforcement with appropriate materials and strict quality control. Additionally, minimizing surcharges on the upper slope is essential to prevent mid-slope damage from excessive loads and maintain overall slope integrity.

Discussion

Theoretical basis and effectiveness of prevention measures

The proposed drainage ditch system is consistent with previous studies Wang et al., indicating that surface water interception can reduce rainfall infiltration by 30–50% in loess slopes¹⁵. However, field studies by Li et al. in the Chinese Loess Plateau show that the effectiveness of this measure may decrease under extreme rainfall (≥ 50 mm/h)⁷. The application of curing agents can enhance soil cohesion by 20–35% for Huang et al., but their long-term durability under cyclic wet-dry conditions remains unvalidated²⁹. Vegetation protection demonstrates dual benefits: root anchoring increases shear strength by 15–25%, while transpiration reduces pore water pressure²⁵. However, this study focuses on herbaceous vegetation, and the effect of arbor species on deep soil stability requires further verification.

While previous studies¹⁰¹⁹, have highlighted the role of pore pressure and shear strength degradation, this study further elucidates the dynamic coupling between fracture evolution and erosion processes, which has been less quantified in earlier works. The integrated monitoring of moisture, pressure, and deformation reveals how fissures act as preferential channels, accelerating wetting front migration and stress redistribution—a key innovation of this research.

Limitations of existing measure

First, the 1:50 scale indoor model tests in this study have scale discrepancies, making it difficult to fully replicate real hydrological processes such as preferential flow in natural fractures in the field. Second, this study has limitations in single-factor research, as it does not consider the coupling effects of seismic loading or groundwater level fluctuations with rainfall, which may further exacerbate slope failure. Additionally, there is a difference in material variability between the homogeneous loess samples used in the tests and natural loess, which often has a stratified structure and uneven particle size distribution. Furthermore, while the core focus of this study was on the integrated failure mechanism, detailed unsaturated hydraulic properties, soil-water characteristic curves and permeability functions were not fully characterized. Future work would benefit from employing quantitative techniques such as Digital Image Correlation (DIC) for fracture analysis, as well as from more comprehensive hydro-mechanical characterization under multi-factor scenarios.

Model validation and comparative analysis

To enhance the reliability of the conclusions drawn from this study, the experimental results were compared with field investigation data from the Shixiakou landslide Mu et al.²⁸. Field surveys of the landslide indicate that failure initiated with erosion and local collapse at the slope toe, followed by progressive sliding of the mid-upper soil mass, ultimately forming a continuous slip surface. Furthermore, Chang et al.⁹ demonstrated through numerical simulations that the factor of safety of a loess-fill slope under rainfall exhibits a three-phase evolution, corresponding respectively to shallow erosion, saturation of the toe region, and overall sliding. The three-stage response patterns of pore water pressure and horizontal earth pressure recorded in this test align well with those numerical findings, further validating that the test successfully captured the key hydro-mechanical coupling processes. Although a dedicated numerical simulation matching the exact test conditions was not conducted, the above comparisons demonstrate good consistency between the observed failure mechanisms and both field phenomena and existing numerical conclusions, thereby supporting the credibility of the experimental outcomes.

Conclusions

This study systematically investigates the failure mode and mechanism of loess slopes under rainfall conditions through comprehensive indoor model tests. By analyzing monitoring data on volumetric water content, pore water pressure, horizontal earth pressure, and slope deformation, the research reveals that loess fill slopes exhibit a retrogressive failure mode during rainfall. This mode progresses sequentially from the slope toe to the crest, with interconnected failure stages leading to complete instability. The migration of the wetting front in slope soil triggers rapid responses in hydrological and stress parameters, where differential water content distribution and slope erosion drive toe failure, while increased pore water pressure and horizontal stress contribute to partial failure in saturated zones. Fracture evolution accelerates rainwater infiltration and alters internal hydrology, influencing central slope failure. Based on these findings, the study proposes scientific prevention and control measures for design, construction, and operation stages, including quality control, protection facilities, and monitoring systems, to enhance slope stability and mitigate landslide risks, and ensure the safety of human lives, property, and engineering infrastructure.

(1) Rainfall-induced loess slope failure exhibits a retrogressive pattern, characterized by stepwise degradation from the toe to the crest, where each failure stage is dynamically interlinked and cumulative damage ultimately leads to slope collapse. The progressive nature of this failure mode provides a time window for early intervention.

(2) The advancement of the wetting front acts as the primary trigger, driving abrupt changes in volumetric water content, pore water pressure, and horizontal stress. Toe failure is dominated by differential water content distribution and erosion, while failure in the saturated zone is governed by increased pore water pressure and horizontal stress. Fracture development promotes preferential flow, accelerating rainfall infiltration and disrupting the internal hydrological balance, which is critical to central slope failure.

(3) The proposed multi-stage prevention measures, encompassing design, construction, and operation, integrate hydrological-stress monitoring with structural protection to establish a comprehensive framework for enhancing loess slope safety. Current research limitations include discrepancies in model scale, insufficient analysis of multifactor coupling, and material authenticity, necessitating future studies to focus on field-scale validation, multifield coupling mechanism research, development of intelligent early warning systems, and long-term performance monitoring to address these gaps.

Data availability

The authors confirm that the data supporting the findings of this study are available within the article.

Received: 20 November 2025; Accepted: 29 January 2026

Published online: 06 February 2026

References

1. Tang, H. Advance and prospects of major landslides prediction and forecasting. *Bull. Geol. Sci. Technol.* **41**, 1–13. <https://doi.org/10.19509/j.cnki.dzqk.2022.0203> (2022).
2. Wang, G., Sun, P., Wu, L., Shi, L. & Zhu, E. Experimental study on mechanism of shallow loess landslides induced by rainfall. *J. Eng. Geol.* **25**, 1252–1263. <https://doi.org/10.13544/j.cnki.jeg.2017.05.010> (2017).
3. Zhong, S. Study on the permeability influence of rainfall on landslide soil. Master's Thesis, Chengdu University of Technology (2015).
4. Yang, Z. et al. Research status and prospect of regional landslide assessment integrating slope deformation characteristics in the complex mountainous area. *Geology China*, 1–13 (2024).

5. Wu, C., Luo, Y., Chen, W. & Li, D. Indoor model experiment for rainfall effects on bare loess slope shape. *Bull. Soil Water Conserv.* **33**, 115–119. <https://doi.org/10.13961/j.cnki.stbctb.2013.01.049> (2013).
6. Lin, H. The study on the mechanism and numerical analysis of rainfall-induced soil slope failure. Ph.D. Thesis, Tsinghua University (2007).
7. Li, M., Zhang, X., Yang, Z., Yang, T. & Pei, X. The rainfall erosion mechanism of high and steep slopes in loess tablelands based on experimental methods and optimized control measures. *Bull. Eng. Geol. Environ.* **79**, 4671–4681. <https://doi.org/10.1007/s10064-020-01854-3> (2020).
8. Xue, J. & Gavin, K. Effect of rainfall intensity on infiltration into partly saturated slopes. *Geotech. Geol. Eng.* **26**, 199–209. <https://doi.org/10.1007/s10706-007-9157-0> (2008).
9. Chang, Z. et al. Experimental study of the failure mode and mechanism of loess fill slopes induced by rainfall. *Eng. Geol.* **280**, 105941. <https://doi.org/10.1016/j.enggeo.2020.105941> (2021).
10. Wu, L. et al. Laboratory characterization of rainfall-induced loess slope failure. *Catena* **150**, 1–8. <https://doi.org/10.1016/j.catena.2016.11.002> (2017).
11. Yao, Y., Yao, L. & Yuan, B. Analysis of a centrifugal model of slope damage mechanism during rainfall. *China Railway Sci.* **25**, 65–69 (2004).
12. Tang, M., Luo, Q. & Hua, Z. Centrifugal model study on the influence of water content on deformation characteristics of high soil cutting slopes. *Subgrade Engineering* 59–62 (2006).
13. Wang, G. & Sassa, K. Factors affecting rainfall-induced flowslides in laboratory flume tests. *Géotechnique* **51**, 587–599. <https://doi.org/10.1680/geot.2001.51.7.587> (2001).
14. Wang, G. & Sassa, K. Pore-pressure generation and movement of rainfall-induced landslides: effects of grain size and fine-particle content. *Eng. Geol.* **69**, 109–125. [https://doi.org/10.1016/S0013-7952\(02\)00268-5](https://doi.org/10.1016/S0013-7952(02)00268-5) (2003).
15. Wang, S., Idinger, G. & Wu, W. Centrifuge modelling of rainfall-induced slope failure in variably saturated soil. *Acta Geotech.* **16**, 2899–2916. <https://doi.org/10.1007/s11440-021-01169-x> (2021).
16. Li, H., Wu, L., Huang, R. & Wang, Y. Physical model tests of two-layer soil slopes under rainfall. *J. Yangtze River Sci. Res. Inst.* **29**, 102–107 (2012).
17. Ren, X. et al. Influence of tension cracks on moisture infiltration in loess slopes under high-intensity rainfall conditions. *Sci. Rep.* **15**, 4488. <https://doi.org/10.1038/s41598-025-88865-w> (2025).
18. Ma, J. et al. Field research on preferential infiltration in rainfall-induced loess landslides. *Eng. Geol.* **354**, 108184. <https://doi.org/10.1016/j.enggeo.2025.108184> (2025).
19. Fan, J. et al. Study on the disaster mechanism and prevention technology of embankment slip-collapse after extreme rainfall in the loess area. *Sci. Rep.* **15**, 20613. <https://doi.org/10.1038/s41598-025-04920-6> (2025).
20. Liu, X. et al. Instability mechanism of loess-mudstone landslides under rainfall infiltration conditions. *Sci. Rep.* **15**, 17591. <https://doi.org/10.1038/s41598-025-01887-2> (2025).
21. Sasahara, K. & Sakai, N. Development of shear deformation due to the increase of pore pressure in a sandy model slope during rainfall. *Eng. Geol.* **170**, 43–51. <https://doi.org/10.1016/j.enggeo.2013.12.005> (2014).
22. Shi, G. et al. Instability mechanism and control measures of loess slope induced by heavy rainfall. *Earth. Surf. Proc. Land.* **50**, e70088. <https://doi.org/10.1002/esp.70088> (2025).
23. Duan, G. et al. Stability analysis of unsaturated loess slopes subjected to extreme rainfall incorporating creep effects. *Comput. Geotech.* **169**, 106231. <https://doi.org/10.1016/j.compgeo.2024.106231> (2024).
24. Liu, W. et al. Rainfall- and irrigation-induced landslide mechanisms in loess slopes: an experimental investigation in Lanzhou, China. *Atmosphere*, **15**, 162. <https://doi.org/10.3390/atmos15020162> (2024).
25. Chae, B. G. & Kim, M. I. Suggestion of a method for landslide early warning using the change in the volumetric water content gradient due to rainfall infiltration. *Environ. Earth Sci.* **66**, 1973–1986. <https://doi.org/10.1007/s12665-011-1423-z> (2012).
26. Zhou, C. et al. Extreme rainfall events triggered loess collapses and landslides in Chencang District, Shanxi, China, during June–October 2021. *Water* **16**, 2279. <https://doi.org/10.3390/w16162279> (2024).
27. Lei, A. & Tang, K. Rainfall similarity in soil erosion model experiments and its implementation. *Chin. Sci. Bull.* **40**, 2004–2006 (1995).
28. Mu, P., Dong, L. & Wu, W. Forming mechanism and stability analysis of Shixiakou landslide at Jiuzhou, Lanzhou. *Northwest. Seismological J.* **30**, 332–336 (2008).
29. Huang, Z., Law, K. T., Liu, H. & Jiang, T. The chaotic characteristics of landslide evolution: a case study of Xintan landslide. *Environ. Geol.* **56**, 1585–1591. <https://doi.org/10.1007/s00254-008-1256-6> (2009).

Acknowledgements

We thank our colleagues at Institute of Geo-environmental Monitoring of China Gansu Province for their great help in this work.

Author contributions

Conceptualization, Y. L., Y. H. and P. L.; methodology, P. L. and Y. L.; validation, G. D. and Y. H.; formal analysis, Y. X., G. D. and M. T.; investigation, Y. H., J. L. and Y. L.; writing—original draft preparation, Y. X., Y. L. and Q. Z.; writing—review and editing, Q. Z., M. T. and Y. X.; funding acquisition, Y. L., Y. H., G. D. and J. L. All authors have read and agreed to the published version of the manuscript.

Funding

This work was supported by the Special Fund for Basic Scientific Research Business of Central Universities (lzujbky-2024-ou03), National College Students' Innovation and Entrepreneurship Training Program (202410730127), The 2023 Innovation Fund Project of Gansu Provincial Bureau of Geology and Mineral Exploration & Development (2023CX18), Central Government's Science and Technology Development Guidance Fund for Local Areas Project (23ZYQA0326), Science and Technology Innovation Project of Department of Natural Resources of Gansu Province (202406), Opening Fund of Technology Innovation Center for Geohazard Monitoring and Early Warning in Gansu Province (2024PT03-05).

Declarations

Competing interests

The authors declare no competing interests.

Additional information

Correspondence and requests for materials should be addressed to P.L.

Reprints and permissions information is available at www.nature.com/reprints.

Publisher's note Springer Nature remains neutral with regard to jurisdictional claims in published maps and institutional affiliations.

Open Access This article is licensed under a Creative Commons Attribution-NonCommercial-NoDerivatives 4.0 International License, which permits any non-commercial use, sharing, distribution and reproduction in any medium or format, as long as you give appropriate credit to the original author(s) and the source, provide a link to the Creative Commons licence, and indicate if you modified the licensed material. You do not have permission under this licence to share adapted material derived from this article or parts of it. The images or other third party material in this article are included in the article's Creative Commons licence, unless indicated otherwise in a credit line to the material. If material is not included in the article's Creative Commons licence and your intended use is not permitted by statutory regulation or exceeds the permitted use, you will need to obtain permission directly from the copyright holder. To view a copy of this licence, visit <http://creativecommons.org/licenses/by-nc-nd/4.0/>.

© The Author(s) 2026